Article

Design and Validation of a New Tilting Rotor VTOL Drone: Structural Optimization, Flight Dynamics and PID Control

Haixia Gong [*] , Wei He [*] , Shuping Hou , Ming Chen , Ziang Yang , Qin Si , Deming Zhao

Article

Design and Validation of a New Tilting Rotor VTOL Drone: Structural Optimization, Flight Dynamics and PID Control

Haixia Gong *, Wei He *, Shuping Hou, Ming Chen, Ziang Yang, Qin Si and Deming Zhao

Mechanical and Electrical Engineering College, Harbin Engineering University

* Correspondence: gonghaixia@hrbeu.edu.cn (H.G.); 10186326@hrbeu.edu.cn (W.H.)

Abstract: This study addresses the gap in experimental validation of tilt-rotor vertical take-off and landing (VTOL) UAVs by developing a novel prototype that integrates fixed-wing and multi-rotor advantages. A dynamic model based on the "X" quadrotor configuration was established, and Euler parameters were employed to derive the attitude transformation matrix. Structural optimization using hybrid meshing and inertia release methods revealed a maximum deformation of 57.1 mm (2.82% of half-wingspan) and stress concentrations below material limits (379.21 MPa on fasteners). The landing gear was optimized via a unified objective method, achieving a 33% reduction in equivalent stress. Vibration analysis identified hazardous frequencies (11–12 Hz) to avoid resonance. A PID control system with DSP28377D demonstrated stable motor speed tracking (±5 RPM) and roll attitude control (<10% error). Experimental validation in low-altitude flights confirmed the prototype's feasibility, though ground effects impacted pitch/yaw performance. This work provides critical experimental data for future tilt-rotor UAV development.

Keywords: tilt-rotor VTOL UAV; structural optimization; vibration analysis; PID control; flight dynamics; experimental validation

1. Introduction

The maximum speed of conventional helicopters is limited by aerodynamic constraints, installed engine power, and airframe drag [1], and problems related to installed engine power and airframe drag can be minimized by careful design, but the main factor limiting the maximum speed of helicopters is the backward paddle stall, and conventional fixed-wing UAVs require a long flight distance for takeoff [2], coupled with increasingly complex integrated mission scenario demand conditions, the shortcomings of conventional fixed-wing UAVs and multi-rotor UAVs are gradually magnified.

In order to make up for the respective shortcomings of fixed-wing and multi-rotor UAVs, UAV scholars have begun the research of combining the advantages of the two types of UAVs, and the concept of vertical take-off and landing (Vertical Take-off and Landing (VTOL) UAVs has been put forward [3,4], which combines the vertical lift of helicopters and the speed and range of fixed-wing aircrafts, and has a wide range of applications in both military and civilian fields [5]. It has a wide range of applications in both military and civil fields [5], especially the tilt-rotor UAV has made more progress after a long period of development. Bell completed the development of "Hawkeye" prototype in 1998, "Hawkeye" adopts the tilt technology of V-22, also loaded with two rotor systems at both ends of the wing, for the tilt-rotor dual rotor UAV, the rotor power is provided by the Allison 250-C20 turbine engine loaded in the fuselage. The rotors are powered by Allison 250-C20 turbine engines mounted on the fuselage, which can complete a 90° forward tilt in flight. The Korean TR-60 is similar in appearance to the Hawkeye, with a rotary engine in each rotor nacelle to control the propeller tilt, and the power is provided by a drive shaft connected to the engine, with a maximum speed of 250km/h [6]. In terms of theoretical studies, S.M. Barkai [7] et al. investigated the

aerodynamic stability model of a tilting rotor using numerical methods and carried out an eigenvalue analysis of the nonlinear periodic correction solution for the model. Christos Papachristos [8] et al. designed a tilting dual-rotor prototype and carried out the nonlinear/linear dynamics of the rotor mode as well as the corresponding attitude tracking controller design, and the control effect of this prototype controller in hovering was verified through experiments. Chowdhury [9] et al. designed a proportional differential (PD) controller based on backstepping for position and attitude control, and the simulation results proved the stability in hovering experiments and the convergence of the system in tracking experiments. Daniel N. Cardoso [10] et al. proposed a new controller for a tilting rotating bi-rotor UAV proposed a novel robust adaptive hybrid control method to handle linear parameter variations. In literature [11,12], researchers designed a quadcopter that allows its rotors to be tilted around the main axis, and the maneuverability and trajectory tracking capability of the UAV was improved. In literature [13,14] the rotor and wing of the vehicle can be tilted together, which reduces the impact caused by wing shading. For the control drive mode of the UAV, most of the current tilt-rotor vertical take-off and landing UAVs use underdriven control schemes, however, the current research on tilt-rotor UAVs is mainly in the area of theoretical analysis and validation, and lack of prototype experimental validation.

In this paper, after analyzing the advantages and disadvantages of various UAVs, based on the lack of experimental prototypes in the field of tilt-rotor vertical take-off and landing UAVs, we combine dynamic modeling and analysis with optimization of the structural control parameters of the experimental machine, and use vibration characteristic analysis to reduce and eliminate the dangers of tilt-rotor vertical take-off and landing UAVs when they are in operation. However, the tilt-rotor vertical take-off and landing UAV has more complex characteristics than conventional flight, and its flight control has a high degree of sub-linearity and coupling, and there are a large number of uncertain interferences in the flight process, PID control methods have been widely used in engineering practice [15], but the traditional PID control methods have limited anti-interference ability, so the use of a better control method to obtain a better experimental aircraft control performance is also a part of this study, the common control parameters of the experimental aircraft, the vibration parameters of the experimental aircraft are optimized. is part of this research, common control methods in the field of UAV are sliding film control [16], adaptive control [17], model predictive control [18], linear-quadratic regulator control [19,20], and serial PID control [21], etc. In this paper, we use serial PID control to control the experimental machine operation, and control data of the attitude of roll, pitch and yaw are collected through the vertical takeoff and landing experiments of the experimental machine. The control data of roll, pitch and yaw attitude are collected and calibrated through the vertical take-off and landing experiments of the experimental aircraft, and finally optimized to get the best control effect and control parameters. The ultimate goal of this paper is to make up for the shortcomings of the tilt-rotor vertical takeoff and landing UAV in the experimental field, and to obtain experimental data that can provide guidance for the research of the tilt-rotor vertical takeoff and landing UAV. The main contributions of this paper include:

1. firstly, a tilt-rotor aircraft with a quad-rotor airframe layout is introduced and dynamically modeled with respect to the requirements of the flight characteristics of a tilt-rotor vertical take-off and landing UAV.

2. In addition, the dynamic characteristics of the landing gear are analyzed for the landing characteristics of vertical take-off and landing UAVs and lightweight requirements, and it is proposed to optimize the landing gear structure by adopting the unified objective method, and to optimize the main motor seat and wing ribs of the UAV by means of the topology optimization module in workbench.

3. The vibration characteristics of the test aircraft body are analyzed, and it is propose d to introduce the harmonic response analysis method to determine the hazardous excitation frequency point of the final tilt-rotor vertical take-off and landing UAV flight.

4. Finally, for the phenomenon that the tilt-rotor vertical take-off and landing UAV is subjected to a lot of interference during its operation, the series PID control method is proposed to collect simulation data and experimental data on the flight attitudes of the experimental aircraft, such as roll, pitch and yaw, to select and optimize the control scheme, and then carry out experiments on the basis of the optimized control scheme to obtain experimental data and draw conclusions for the research of the tilt-rotor vertical take-off and landing UAV. Provide experimental data with reference and guidance.

2. Complete UAV Design

2.1. Dynamic Modeling

The tilt-rotor UAV of this design is different from the known tilt-rotor UAVs, which is designed with four rotors, and the middle wing is loaded with the main rotor, which provides the main lift for the UAV in the multi-rotor flight mode, and it can be tilted (0~90) degrees during the flight process, and the tail rotor is a fixed rotor, which can't be tilted, and it is mainly used to provide the UAV with part of the lift in the multi-rotor flight mode and cooperate with the main rotor to realize the UAV vertical takeoff and landing and flight attitude change. The dynamics model of the tilt-rotor UAV is similar to the "X" quadrotor UAV in flight state, as shown in Figure 1, the four rotors are matched with different rotational speeds so as to realize the UAV's four flight states of altitude control, pitch, roll and yaw.
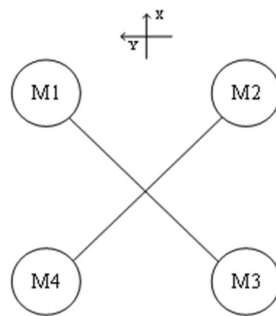

Figure 1. X-mode quad copter drone.

The two coordinate systems, ground coordinate system and airframe coordinate system, are established to describe the motion state in the air for the UAV spatial coordinate system. Again based on this, Euler angles and x, y, z are defined to jointly describe the attitude and position of the UAV, where the Euler angles are the pitch θ, roll ϕ and yaw ψ angles, respectively. Thus, the overall transformation matrix is obtained:

$$R(\phi,\theta,\psi) = \begin{bmatrix} \cos\theta\cos\psi & \sin\phi\sin\theta\cos\psi - \cos\phi\sin\psi & \cos\phi\sin\theta\cos\psi + \sin\phi\sin\psi \\ \cos\theta\sin\psi & \sin\phi\sin\theta\sin\psi + \cos\phi\cos\psi & \cos\phi\sin\theta\sin\psi - \sin\phi\cos\psi \\ -\sin\theta & \sin\phi\cos\theta & \cos\phi\cos\theta \end{bmatrix} \quad (1)$$

Assume that the UAV is a rigid body and does not undergo deformation, that the origin of the camera coordinates of the UAV coincides with the center of mass, that the rotation and revolution of the earth are neglected, and that the takeoff plane is horizontal. The UAV dynamics equations are obtained:

$$\vec{F}_B = \vec{F}_1 + \vec{F}_2 + \vec{F}_3 + \vec{F}_4 \quad (2)$$

$$\tilde{\vec{F}}_E = R(\phi,\theta,\psi) \cdot \tilde{\vec{F}}_B \quad (3)$$

$$
\begin{cases}
\ddot{x} = \frac{1}{m}\left[\cos\theta\sin\psi\sin\phi\sin\theta\cos\psi - \cos\phi\sin\psi\cos\phi\sin\theta\cos\psi + \sin\phi\sin\psi\right]\vec{F}_B \\[2mm]
\ddot{y} = \frac{1}{m}\left[\cos\theta\sin\psi\sin\phi\sin\theta\sin\psi + \cos\phi\cos\psi\cos\phi\sin\theta\sin\psi - \sin\phi\cos\psi\right]\vec{F}_B \\[2mm]
\ddot{z} = \frac{1}{m}\left[-\sin\sin\phi\cos\theta\cos\phi\cos\theta\right]\vec{F}_B - g \\[2mm]
\ddot{\phi} = \dot{\theta}\dot{\psi}\frac{I_y - I_z}{I_x} + \left(\vec{F}_1\cdot\vec{l}_1 + \vec{F}_4\cdot\vec{l}_4 - \vec{F}_2\cdot\vec{l}_2 - \vec{F}_3\cdot\vec{l}_3\right)/I_x \\[2mm]
\ddot{\theta} = \dot{\phi}\dot{\psi}\frac{I_z - I_x}{I_y} + \left(\vec{F}_1\cdot\vec{l}_1 + \vec{F}_2\cdot\vec{l}_2 - \vec{F}_3\cdot\vec{l}_3 - \vec{F}_4\cdot\vec{l}_4\right)/I_y \\[2mm]
\dot{\psi} = \dot{\theta}\dot{\phi}\frac{I_x - I_y}{I_z} + \left(d_1\cdot\vec{F}_1 + d_3\cdot\vec{F}_3 - d_2\cdot\vec{F}_2 - d_4\cdot\vec{F}_4\right)/I_z
\end{cases}
\tag{4}
$$

where each parameter: $\vec{F}_1$、$\vec{F}_2$、$\vec{F}_3$、$\vec{F}_4$ is the lift generated by the rotor; $\ddot{x}$、$\ddot{y}$、$\ddot{z}$ corresponds to the acceleration on the three coordinate axes; m is the mass of the UAV; I_x、I_y、I_z is the inertia of the air-frame; $\vec{l}_1$、$\vec{l}_2$、$\vec{l}_3$、$\vec{l}_4$ is the force arm from the center of the rotor to the origin of the air-frame coordinate system; d_1、d_2、d_3、d_4 is the performance parameter of the propeller.

It can be found through the dynamics model that the pitch, roll and yaw attitude control of the tilt-rotor concept UAV in multi-rotor mode is related to its mass, rotational inertia, force arm from the rotor to the center of gravity and the lift generated by the power system.

Combined with the rotor momentum theory to analyze the generation and change of airflow, as shown in Figure 2, assuming that the air is an ideal fluid, the rotor is infinitely thin and uniformly in contact with the air, and the airflow is constant at each point of the action disk. To establish a uniform load rotor disk model as shown in Figure 3, B-B cross-section is the rotor disk, A-A cross-section and C-C cross-section are the upstream and downstream boundaries, V_0 is the velocity of the airflow in the 0-0 cross-section, the velocity of the airflow at the B-B cross-section is V_1, and the velocity of the airflow reaches the C-C cross-section, and the velocity increases to V_2, v_1 and v_2 are the induced velocity of the airflow at the two cross-section. The following relation is obtained based on the theorem of momentum, the theorem of conservation of mass, and the theorem of conservation of energy:
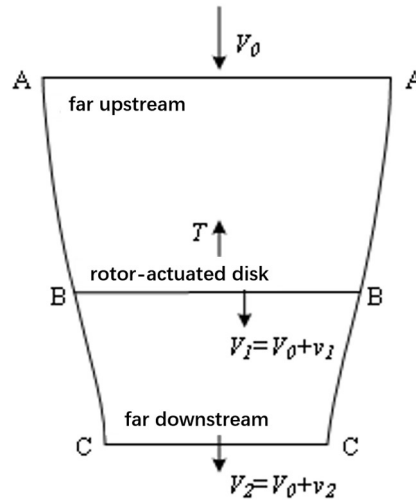
$$
T = T' = m(V_2 - V_0) = mv_2 \tag{5}
$$

Where: T' is the external force acting on the fluid by the rotor, T is the rotor tension; m is the fluid mass; V_0、V_2 the airflow velocity; and v_2 is the local airflow induced velocity far downstream.

$$
m = \rho V_0 S_0 = \rho V_1 S_1 = \rho V_2 S_2 = \text{constant} \tag{6}
$$

(6) where: ρ is the air density; S_0、S_1、S_2 are the upstream distant, action disk, and downstream distant areas, respectively.

Figure 2. Rotor action disk model of momentum theory in vertical rise state.

The power consumed by the rotor is determined by the rate of change of kinetic energy of the fluid within the model:

$$P = m(V_2^2 - V_0^2)/2 = m(V_0 + v_2/2)v_2 \quad (7)$$

Since the rotor power is equal to the product of the rotor pull force and the airflow velocity V_1 at the rotor action disk, expressed as:

$$P = TV_1 = TV_0 + Tv_1 \quad (8)$$

At the rotor action disk, $V_1 = V_0 + v_1$, $S = \pi R^2$, which ultimately gives the relationship between rotor pull and power:

$$T = 2\rho\pi R^2 \left(V_0 - v_1\right)v_1 \quad (9)$$

$$P = 2\rho\pi R^2 (V_0 - v_1)^2 v_1 \quad (10)$$

In multi-rotor mode, the rotor power and lift are only related to the local induced speed and propeller disk area. The effect of the skin of the air-frame on the air-frame can can be directly addressed by the power and speed of the rotor.

2.2. Fuselage Design

The UAV studied in this paper needs to adapt to two working conditions. Working condition one is the ground test of the whole aircraft, mainly testing the remote communication function of the control system and the performance of the power system. Working condition two is to complete the vertical takeoff and landing of the test aircraft and hovering process of pitch, roll, yaw and other attitude control. Taking into account the cost and process characteristics, and at the same time need to meet the mechanical and dynamic performance indicators, the design of the design indicators as shown in Table 1.

Table 1. Design indicators.

parameters	numerical value	parameters	numerical value
fuselage length	3000mm	tail rotor wheelbase	2190mm
fuselage width	548mm	Main tail rotor X-direction wheelbase	1763.7mm
Fuselage height	645mm	Maximum weight of the drone	350 kg
wingspan	4045mm	Maximum main rotor power	160kw
tail spread	2260mm	Tail rotor power	18kw
main rotor wheelbase	3695.4mm	thrust ratio	1.3

According to the requirements, the material selection of the prototype should ensure that the structural strength and stiffness of the basis to achieve the minimum mass, but also need to reduce the cost of the experiment. After comprehensive consideration of material density, tensile modulus, tensile strength, specific modulus, specific strength and other performance indicators, it was decided to use aluminum alloy and titanium alloy UAV body structure materials. The airframe design requires reasonable layout structure, lightweight, easy disassembly and maintenance, safety and economy. Therefore, the overall structure of this design is shown in Figure 3, the test aircraft wing and tail wing are connected to the upper fuselage through cross fasteners, which are distributed and installed at 1015mm and 2809mm from the front end of the fuselage, and the four rotors are installed at the ends of the wing and the tail wing respectively, and the wing parameters refer to the cruise lift coefficient of the same class of fixed-wing aircraft C_{Lwing} (0.8) to obtain the wing area of about 3m², and refer to the twin-engine airplane, which has the following characteristics. The wing chord ratio AR is 12, the C_{ave} is about 0.5m, and the wing length is 6m, the weight of the experimental test aircraft is large, and the wing bears the main propeller tension during the flight, the three-beam structure can satisfy the requirements, the main beam has a sufficiently high strength, and the aileron strength is weaker, according to the structural requirements and the characteristics of the wing, the main beam is located at 26% of the wing chord, and the two aileron beams are located at 8% and 57% of the wing chord respectively. According to the structural requirements and wing characteristics, the main girder is located at 26% of the wing chord length, and the two secondary girders are located at 8% and 57% of the wing chord length.

$$S_{wing} = \frac{Mg}{\rho V C_{Lwing}} \tag{11}$$

(11) Where: S_{wing} is the wing area; M is the whole aircraft design mass; V is the design flight speed.

$$C_{ave} = \sqrt{\frac{S_{wing}}{AR}} \tag{12}$$

$$B = AR \times C_{wing} \tag{13}$$

(12) Where: B is the spread length.

Tail parameter reference weight leveling, using the formula (11), (12) and (14) calculated flat tail area of about 1.0976m². tail structure design to meet the strength and stiffness requirements can be, at the same time to leave enough space for the electronic speed controller. Therefore, the tail structure

form uses double beam type, the two beams l_h have the same structural parameters, are used in the long 2260mm, inner diameter of 44mm, outer diameter of 48mm 6061 aluminum alloy tube, tail two beams spacing is 140mm.

$$V_{ht} = \frac{l_h S_h}{C_{ave} S_{wing}}$$ (14)

(14) Where: l_h is the length from the quarter chord position of the flat tail to the center of gravity; S_h is the area of the flat tail; V_{ht} is the capacity of the flat tail.

The fuselage design takes into account that this experimental aircraft is only used for vertical takeoff and landing and hovering flight, and it is required to be easily disassembled and transported on the basis of cost reduction, so it is selected to be of ko-truss-beam structure, and the landing gear is selected to be the common sled-type landing gear, and the bow-beam and the left and right sled of the landing gear are welded together with the titanium alloy round tubes with the inner diameter of 26mm and the outer diameter of 30mm, and the height of the sled-type landing gear is designed to be 385mm. The height of the skid landing gear is designed to be 385mm, the spacing between skids is designed to be 1166mm, and the spacing between the front and rear bow beams is initially designed to be 800mm.
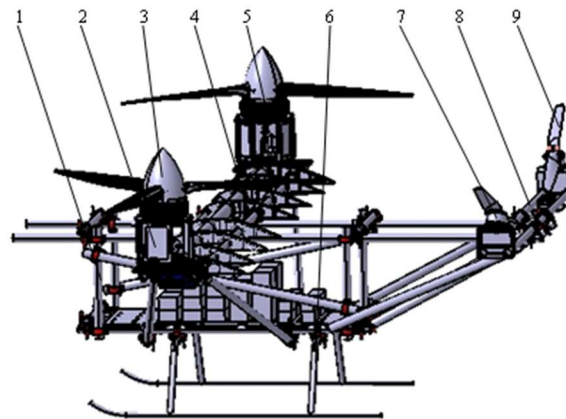
Figure 3. 3D general structure of the tilt-rotor UAV. 1, Fuselage 2, Nacelle 3, Main propeller 4, Wing 5, Main motor 6, Landing gear 7, Tail motor 8, Tail wing 9, Tail propeller.

3. Prototype Structure Optimization

3.1. Static Analysis

The strength and stability of the body structure of the prototype is crucial to the performance of the prototype. The designed model of the prototype body is imported into the analysis software, the prototype fuselage, wings, tail and other related structures are the main load-bearing components of the prototype, which need to be retained, and the bearings, bolts and other parts of the overall impact of the prototype is relatively small, and appropriately simplified. The designed three-dimensional model of the prototype body is imported into Workbench, and tetrahedral meshing is used for the parts with complex structure and small size, hexahedral meshing is used for the structural rules, and the mesh density of the main load-bearing parts is increased appropriately.

According to Table 1, the maximum design weight of the prototype is 350 kg, the design weight of the fuselage is 34.9 kg, the design weight of the wing is 33.5 kg, the design weight of the tail is 6.9 kg, the design weight of the wing powertrain is 117.3 kg, the design weight of the tail powertrain is 20.4 kg, and the design weight of the onboard equipments and the landing gear is 137 kg. The fuselage, wing and tailplane are made of 6061 aluminum, the connecting fasteners are made of ductile cast iron, and the main motor mount connectors are made of structural steel. The main rotor can provide a maximum lift of 1800 N unilaterally, and the tail rotor can provide a maximum lift of 500

N unilaterally. The powertrain, airborne equipment, and landing gear are simplified to be given to the fuselage in the form of force. Taking the safety factor of 1.25, the lift force is 2250 N distributed on both sides of the wing and 625 N distributed on both sides of the tail rotor.

The flight process of the test aircraft has six degrees of freedom, and the constraints are applied by the method of inertial release, assuming it is stationary, to complete the hydrostatic analysis. After the boundary conditions are applied, the static solution of the test aircraft is started, and the results are shown in Figure 4 and Figure 5. From Figure 4, it can be seen that the maximum deformation of the test aircraft occurs at the edge of the wing beam and the main motor seat after the force is applied, and the maximum deformation value is 57.1mm, and the ratio of its half wingspan is about 2.82%, which meets the design requirement of less than 3%, so the stiffness of the test aircraft meets the design requirement; from Figure 5, it can be seen that the maximum equivalent force of the test aircraft body structure is concentrated in the tailplane, and the maximum equivalent force of the test aircraft body structure is concentrated in the tailplane. As can be seen from Figure 5, the maximum equivalent force of the structure is concentrated in the scaffolding fasteners, and the maximum equivalent force value is 379.21 MPa, which is smaller than its minimum strength limit of 450 MPa; the maximum stress concentrated in the aluminum alloy tubes of 6061 and 7075 is 142.2 MPa, which is smaller than its minimum ultimate strength of 240 MPa and 455 MPa, so the structural strength of the prototype meets the design requirements. The 2.82% deformation ratio ensure structural integrity during takeoff/landing.
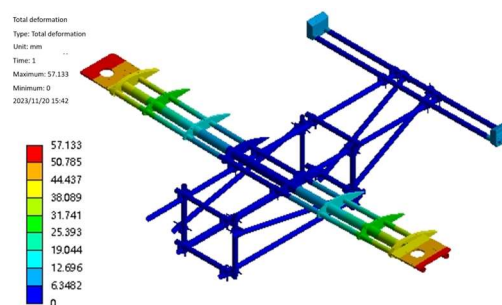
**Figure 4.** Deformation of the body under force.
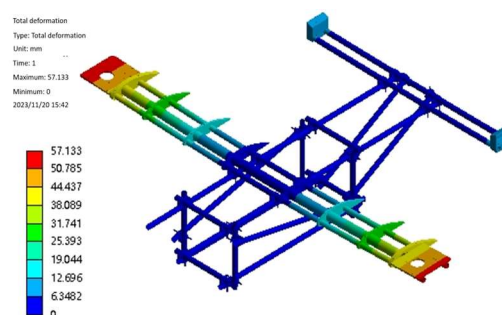
Figure 5. Stresses on the body.

3.2. Optimization of Landing Gear, Wing Ribs and Main Motor Seat

3.2.1. Optimization of Landing Gear Structural Parameters

The landing gear designed in this paper not only wants to have a certain elastic deformation capacity to absorb the impact kinetic energy of the test aircraft landing, but also wants to have enough strength to avoid fracture due to excessive deformation. In the process of designing the landing gear, it is necessary to rationalize the design by combining the UAV design, strength and stiffness requirements. The landing gear is mainly subject to the extreme impact of the test aircraft landing, according to the landing situation, the landing gear will be loaded into two working conditions: when

the landing gear left and right sides to withstand the main force, the safety factor of 1.5, the left and right two joints of the average force of 2625 N; when the landing gear front and rear end to withstand the main force, the front and rear end of the average force of the joints is 2625 N. The analysis results in Figure 6. working condition 1 In Case 1, the front and rear bow beams are mainly subjected to a single force, so the deformation is mainly concentrated in the middle of a single bow beam, and the stress is concentrated on both sides of a single bow beam force point and the connection between the bow beam and the skid; in Case 2, the bow beams are mainly subjected to side force, and the deformation and the stress are mainly concentrated on the side of the bow beams, and the static analysis of the landing gear under both cases meets the requirements of the yield strength.
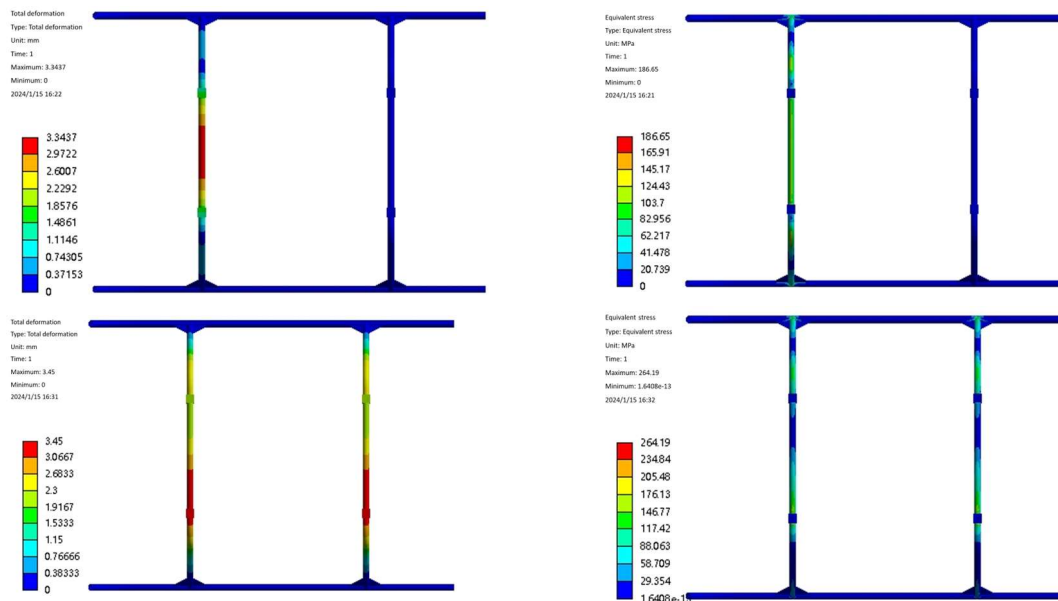
Figure 6. Static force analysis of two working conditions of Landing Gear.

When analyzing the landing gear landing impact, the fuselage mechanism is not considered and the mass point representation is used. The mass point is set at the center of gravity of the fuselage, the four connection points of the landing gear bow girder and the fuselage are used as the mass point connection locations, the constraints are set as rigid body connections, and the attributes of the mass point are set as rigid, and the mass and rotational inertia of the fuselage are assigned to the mass point, and the impacted ground is simulated by a rigid wall. The landing gear finite element model is shown in Figure 7.
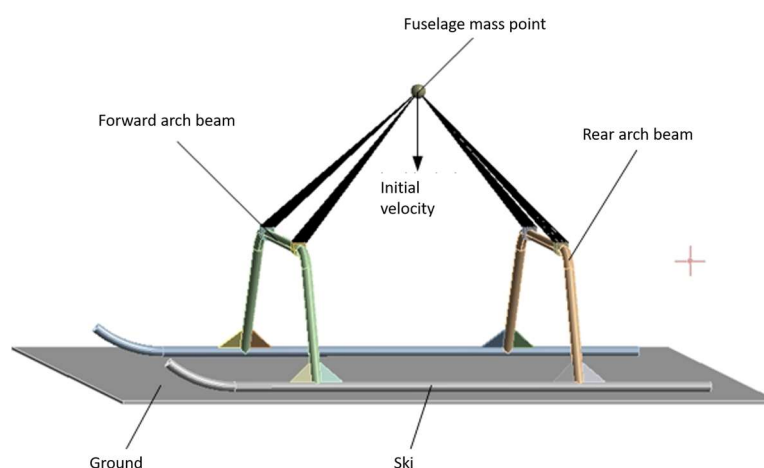
Figure 7. Finite element model of landing impact of skid landing gear.

The time used in the simulation is set to 0.08s, the constraint mode of the skid and the ground model is set to friction, the friction coefficient is set to 0.15, and the landing speed is selected to be 0.15m/s which occurs the most times in the actual airplane, combined with the speed of the maximum of 1.37m/s to do comparisons and analyses, and the appropriate landing speed is selected. When the test aircraft landed at a speed of 0.15m/s, Figure 8 shows the results of the landing gear landing impact simulation and analysis of cloud diagrams, respectively, along the x, y, z-axis direction of the deformation of the cloud diagram and the equivalent force cloud diagram. Figure 9 shows the deformation and equivalent force change curve along the x, y, z direction when landing gear working condition one impact landing.
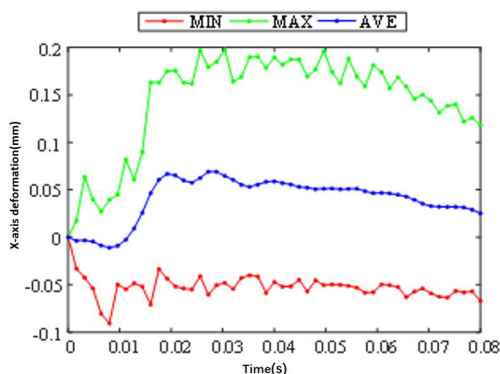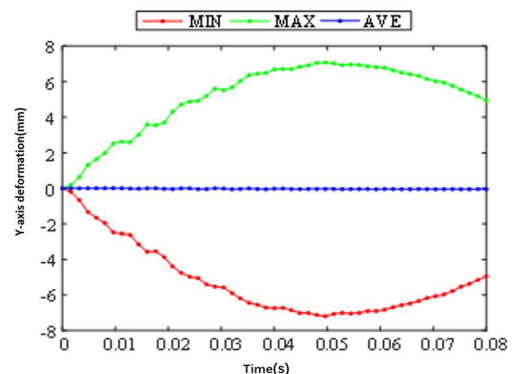

(a)

(b)

(c)

(d)
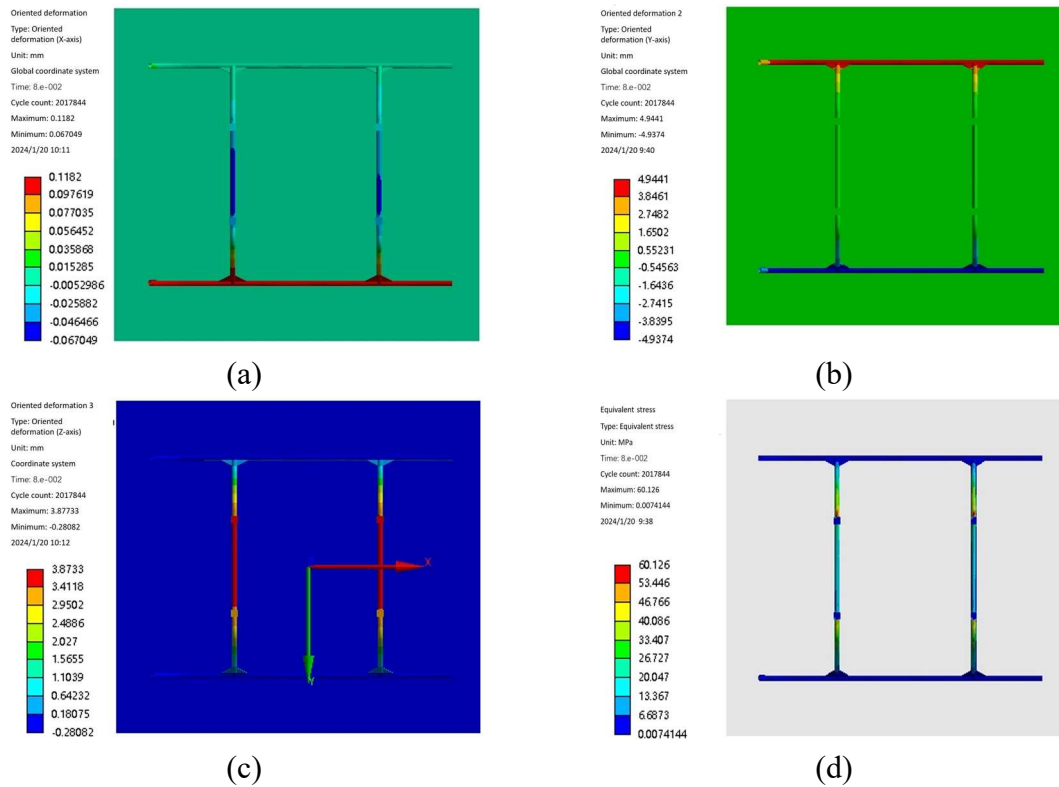
Figure 8. Simulation cloud diagram of landing gear impact for Case 1.

(a) X-direction deformation

(b) Y-direction deformation

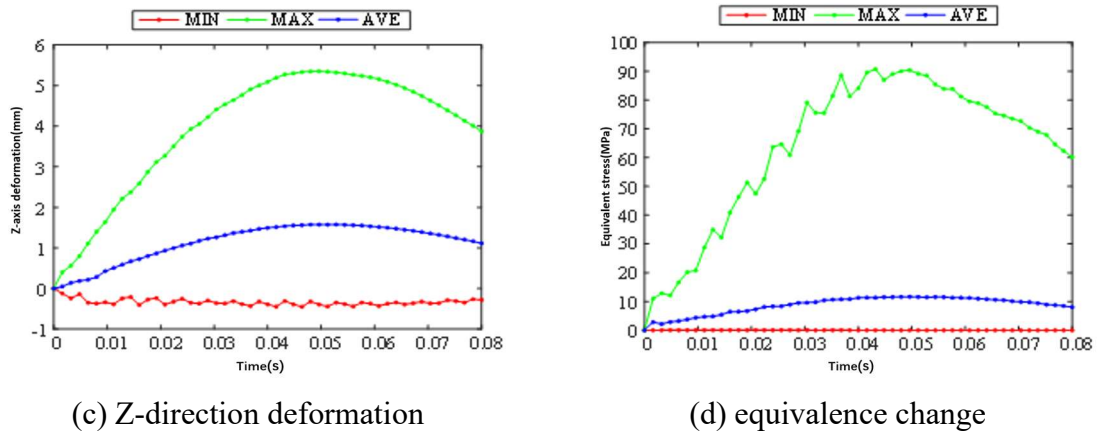(c) Z-direction deformation   (d) equivalence change

Figure 9. Simulation curve of landing gear impact for condition 1.

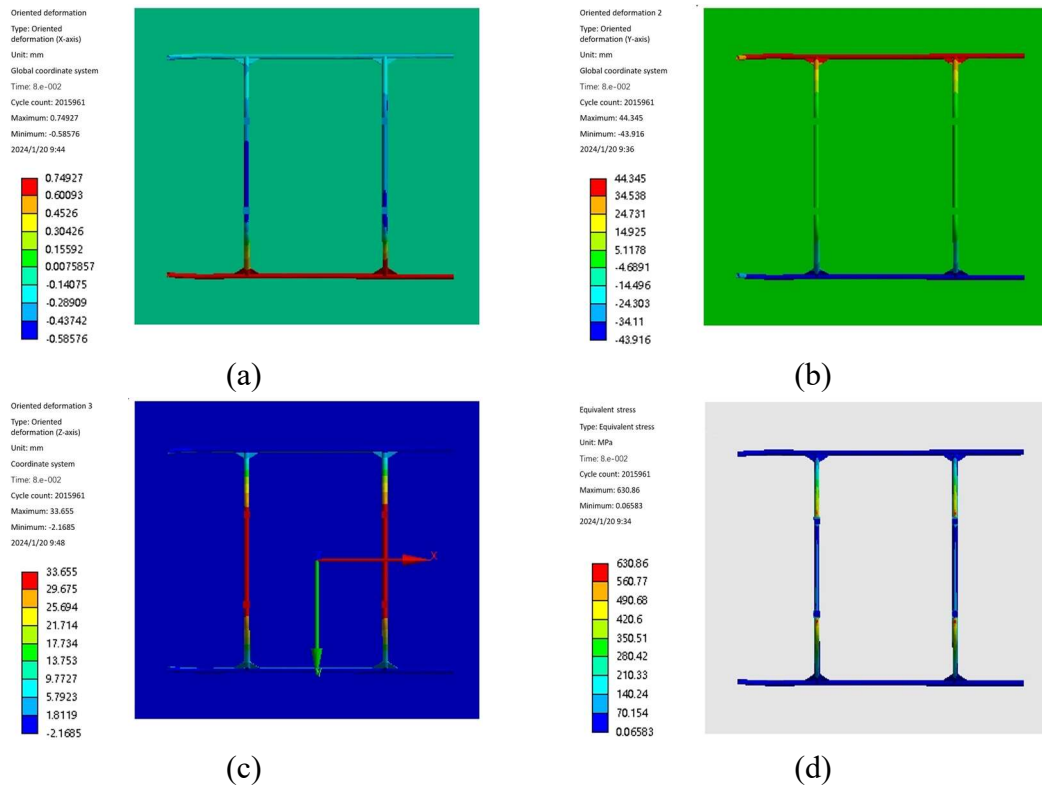The simulation cloud diagram when the prototype landed at maximum speed is shown in Figure 10.

Figure 10. Simulation cloud diagram of landing gear impact in Case 2.

The deformation and equivalent force change curves along the x, y, and z directions during landing gear condition II impact landing are shown in Figure 11.

(a) X-direction deformation

(b) Y-direction deformation

(c) Z-direction deformation

(d) equivalence change
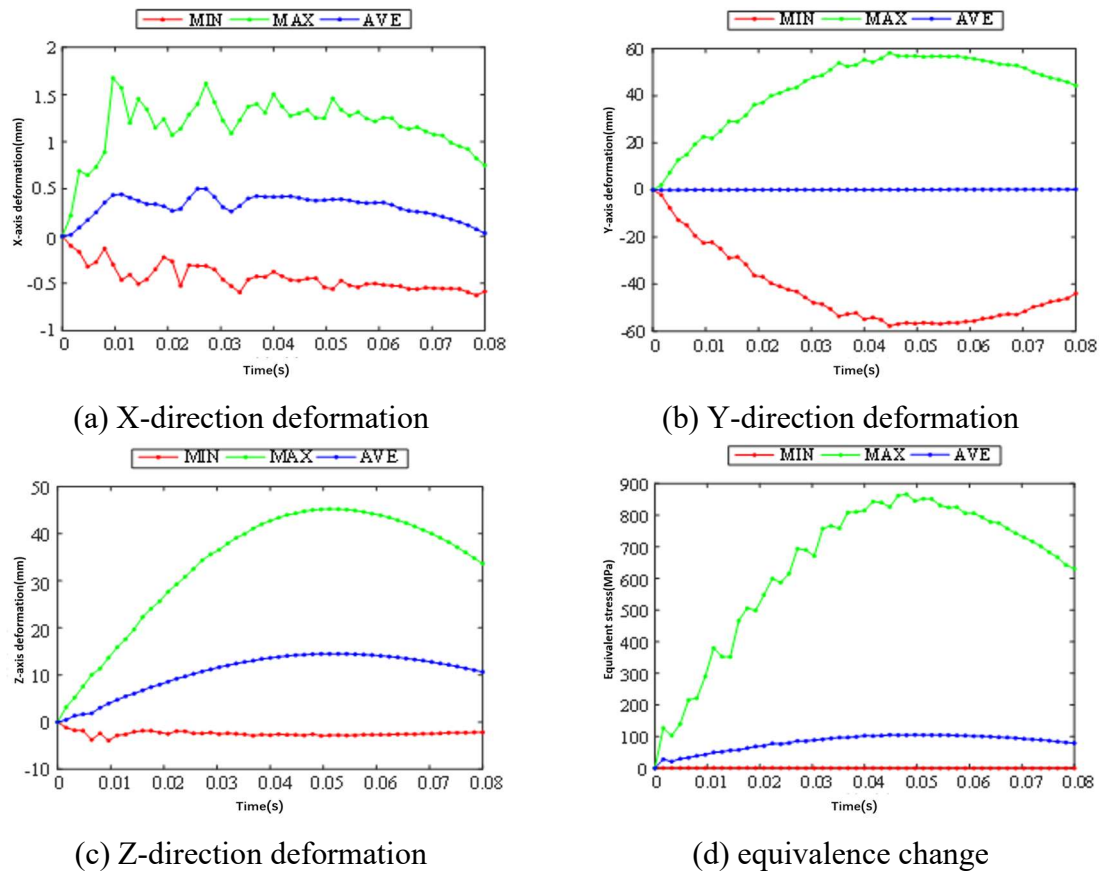
Figure 11. Simulation curve of landing gear impact for working condition 2.

When the landing gear in 0.15m/s speed impact landing, the maximum stress 90.38 MPa is far less than the yield strength of the landing gear 825 MPa. When the landing gear in 1.37m/s speed impact landing, the maximum stress 824.88 MPa is close to the yield strength of the landing gear, in the actual flight should be avoided to 1.37m/s speed landing situation. In order to control the landing gear safety coefficient can reach more than 1.3, so the speed of the test aircraft is controlled between 0.15m/s and 1m/s, which is able to realize a safe landing.

Unified objective method is introduced to iteratively optimize the beam length L and clamp angle in the landing gear, and the multi-objective function of the model can be expressed as follows:

$$\begin{cases} \min F(X) = \min[f_1(X), f_2(X), \cdots, f_j(X)]^T \\ \text{s.t.} \begin{cases} g_u(X) \le 0, (u = 1, 2, \cdots, m) \\ h_u(X) \le 0, (u = 1, 2, \cdots, n) \end{cases} \\ X = [x_1, x_2, \cdots, x_i] \end{cases} \tag{15}$$

Where: $F(X)$ is the objective function; g_u and h_u is the constraint function; X is the target variable.

The combined objective function is obtained by combining the linear weighting method:

$$F(X) = W_1 \cdot f_1(X) + W_2 \cdot f_2(X) + \cdots + W_r \cdot f_s(X) \tag{16}$$

Where: W_r is the weighting factor. It is used to indicate the importance of each objective function with the following relationship:

When optimizing the design variables L and, the maximum equivalent force and the landing gear mass are given priority, and a mathematical model with accurate parameters is obtained. Then the landing gear optimization design is realized through the response surface optimization module in workbench, Solid works and workbench are interacted, the parameterization of the design

variables is carried out in solidworks, and after that the analysis is carried out in finite element software, and the landing gear landing speed is taken as 1m/s. Finally, the response surface module will collect the sample points through the intermediate material method. , the optimization is completed by fitting the samples.

After the optimization of the response surface size, the optimization results are shown in Table 2, the value of the landing gear bow-beam rod length is reduced to 579.15mm, the value of the bow-beam angle is increased to 123.9°, and the overall mass of the landing gear is reduced by 0.037 kg, which is not significant in terms of mass reduction, but the static strength is greatly increased, and the maximum equivalent stress is reduced by 204.08 MPa under the same conditions.

Table 2. Comparison before and after optimization.

Optimization Variables	Bow-beam pole length L (mm)	Bow-beam angle α (°)	Mass m (kg)	maximum equivalent force (physics) σ(MPa)
pre-optimization	600	120	5.795	616.54
post-optimization	579.15	123.9	5.758	412.46

3.2.2. Wing Ribs and Main Motor Mount Optimization

The wing ribs and the main motor seat are optimized using the topology optimization method. Combining the variable density method of the topology optimization module in workbench and the static structure module together to complete the optimization, after importing the 3D models of the main motor seat and the wing ribs into Workbench, the optimization setup is carried out, and the optimization process is shown in Figure 12.
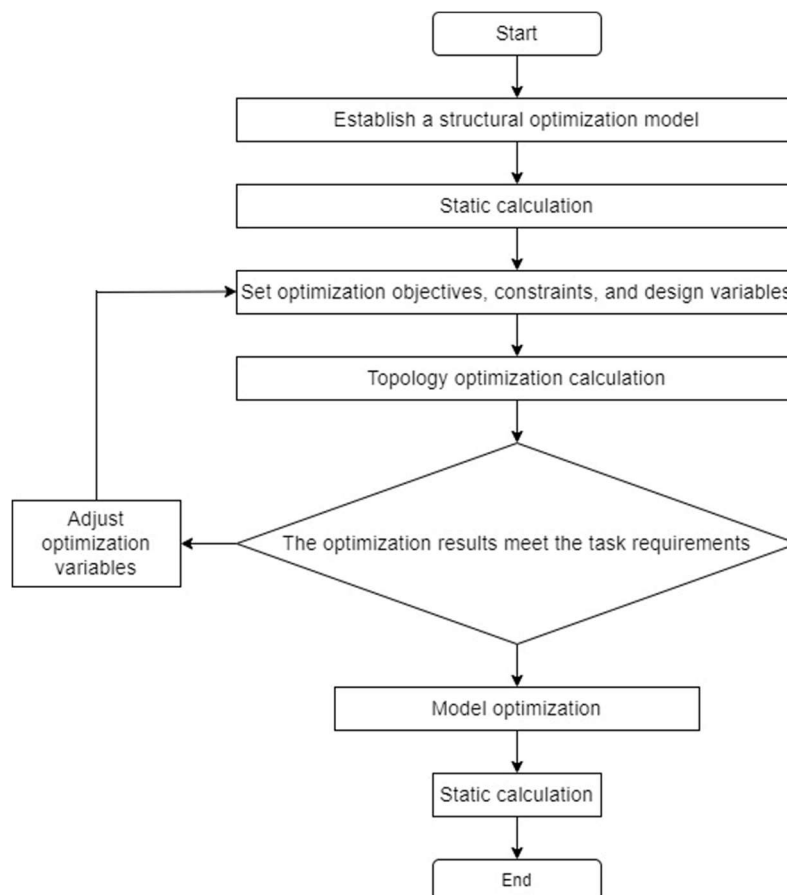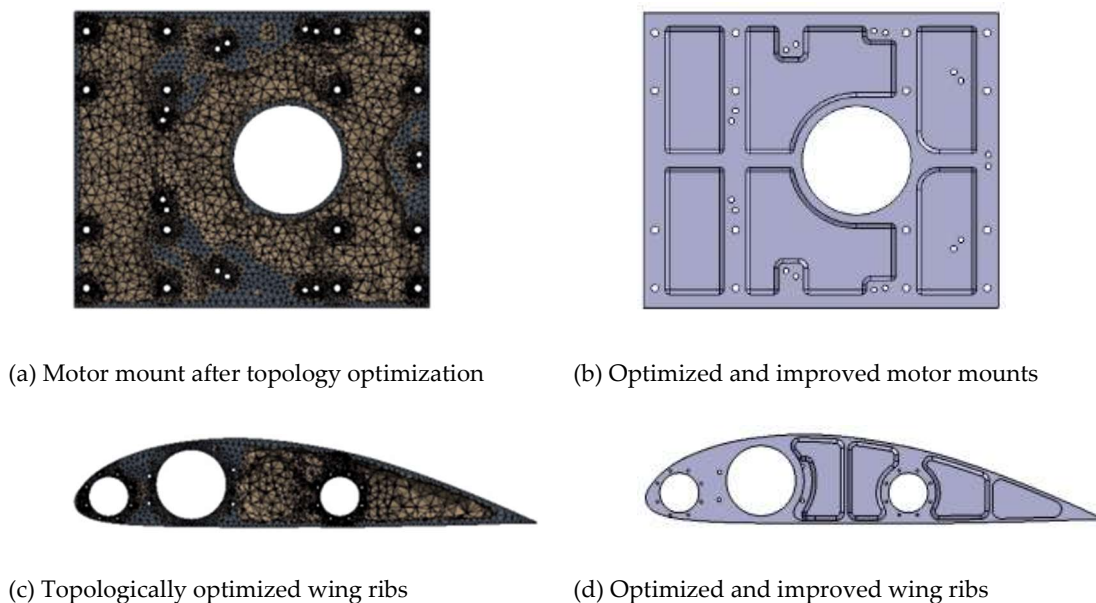

Figure 12. Topology optimization flow.

According to the actual selection of materials, the structural material properties are set up, model meshing, in order to ensure the accuracy of the calculation results, the average mesh quality needs to be greater than 0.7, so the mesh size is selected as 5mm, locally encrypted to 1mm. topology optimization region will be divided into the force transfer structure and bolts and other mounting holes will be divided into non-optimized areas, according to experience to retain the structural reinforcement, the rest of the structure can be divided into optimized areas to get a better optimization effect. According to the experience, the structural reinforcement is retained, and the rest of the structure can be divided into optimized regions to get better optimization effect. Setting the mass percentage as the reference value of constraints, in order to obtain better optimization results, the reference value of motor seat topology optimization is 0.6, and the reference value of wing rib topology optimization is 0.55. The prototype designed in this paper has a total of 8 wing ribs, of which two are reinforcing ribs, and the rest are ordinary ribs. The reinforcing ribs are the main load-bearing components, and the common ribs mainly play the role of stabilizing the main beam of the wing, so the topology optimization of the wing ribs in this section mainly optimizes the reinforcing ribs, and the rest of the wing ribs refer to the optimization results of the reinforcing ribs.

Figure 13(a) and (c) give the design results of the topology optimization of the motor seat and reinforcing ribs of the prototype, and the optimal material distribution of the motor seat mass and the reinforcing ribs at the smallest time under the given constraints. The optimization yields a clearer shape of the motor seat and reinforcing wing rib parts. In the actual manufacturing process, the feasibility of parts processing should be taken into account, in addition, in the assembly process, since the mounting holes need to withstand the transferred loads, so it is necessary to retain a certain amount of material to ensure its strength. Taking these factors into consideration, the optimized structure of the mitigation groove of the motor seat and wing rib is improved again, firstly, the irregular shape of the edge of the mitigation groove needs to be smoothed and processed, so as to make it easy to process and to prevent stress concentration, and then the mitigation groove with less material removal needs to be deleted appropriately according to the demand, and the modified parts are shown in Figure 13 (b) and (d).

(a) Motor mount after topology optimization   (b) Optimized and improved motor mounts

(c) Topologically optimized wing ribs   (d) Optimized and improved wing ribs

**Figure 13.** Optimization of structural components.

The optimized model is subjected to strength verification, and the mechanical finite element analysis is used to obtain that the maximum deformation of the motor seat after topology optimization and design modification is 0.08mm, and the maximum stress is 26.86 MPa, which occurs in the position of the bolt holes of the motor connection. The maximum deformation of the optimized

wing ribs is 0.02mm, and the maximum stress is 12.94 MPa, which mainly occurs at the position of the contact surface of the main and secondary beams, and combined with the space of the safety coefficient of the structure, the optimization results meet the experimental requirements.

4. Vibration Characterization of the Prototype

The vibration response characteristics of the prototype are analyzed in both free and restrained modes, and the modal analysis is solved by the lumped Lansos method in workbench. The free and restrained modes are selected to analyze the modes with the first 80% of the effective participating mass, and the first twelve orders of the vibration mode cloud are selected to analyze the vibration mode characteristics of the prototype. The shaft frequency in the free mode is close to the 10th and 11th order intrinsic frequencies of the machine, but the vibration characteristics of the structure tend to be greater in the lower order modes, so it can be assumed that resonance does not occur in the free mode. The test in the constrained mode is mainly a ground performance test, in the workbench to impose boundary conditions on the test model, the material is given and the mesh delineation steps are the same as the free mode analysis of the airframe, the excitation frequency generated by the propeller and the airframe of the first twelve constrained modes have more than one intrinsic frequency close to the resonance of the possibility of resonance, but also need to be harmonic corresponding to determine the corresponding analysis However, a harmonic correspondence analysis is needed to determine whether the airframe resonates in the constrained state.

Harmonic response analysis calculates the corresponding deformation, stress and strain response curves of the structure in different frequency ranges, which can get the vibration danger point of the mechanical structure, and the frequency range needs to be determined according to the intrinsic frequency and the excitation frequency of the mechanical structure, and the modal analysis prior to the harmonic response analysis provides important information about the vibration characteristics for the harmonic response analysis. This section analyzes the dynamic response of the body structure under the action of sinusoidal harmonic excitation load, and analyzes and solves the "amplitude-frequency" response curve of the body, as shown in Figures 14 and 15.
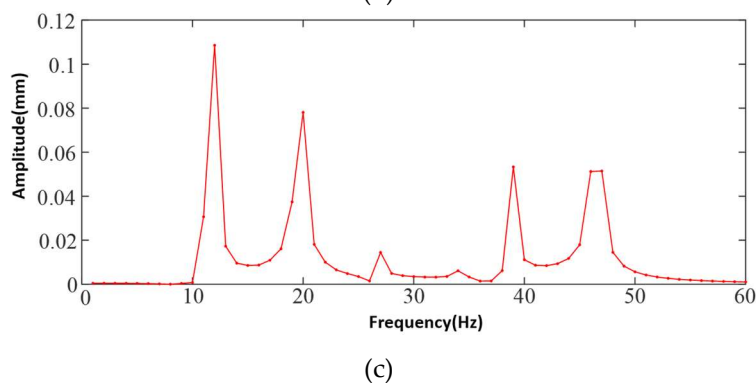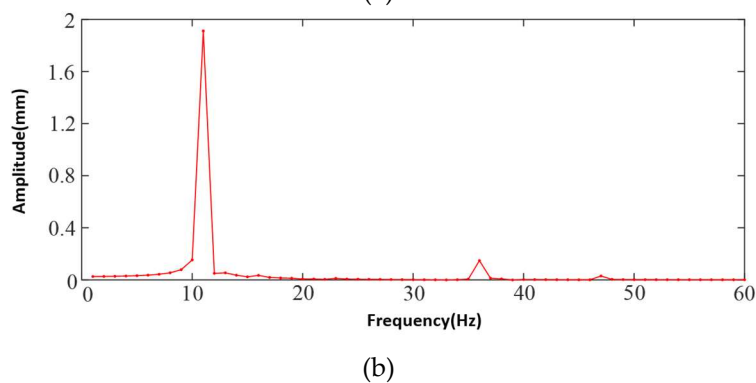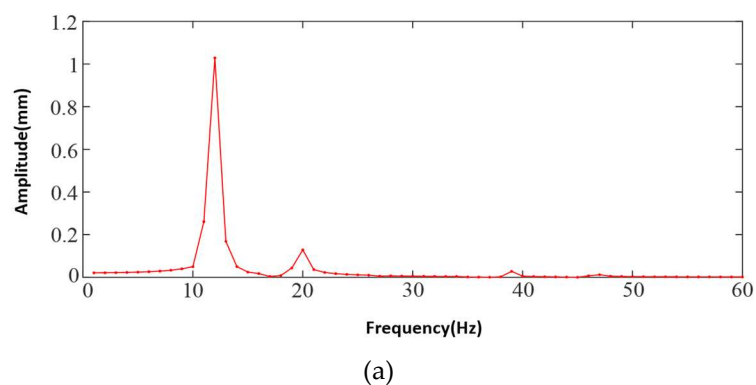

(a)

(b)

(c)
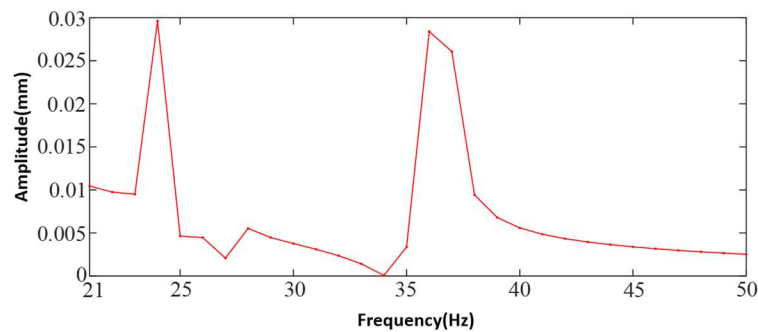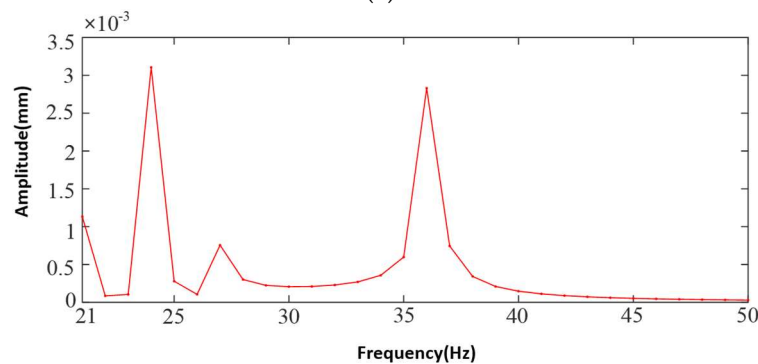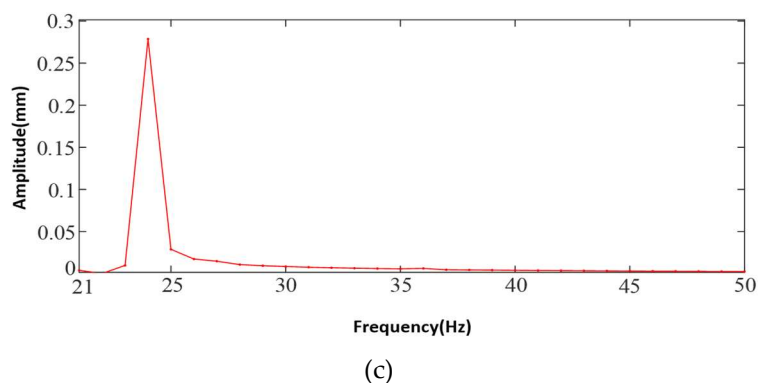
Figure 14. Harmonic response analysis in free mode.

(a)

(b)

(c)

Figure 15. Harmonic response analysis under constrained modes.

Analyzing the harmonic response characteristics of the free mode, when the excitation frequency is 24Hz, the vibration of x, y, z direction has the greatest influence, and the amplitude of the vibration in the z direction reaches the maximum of 0.28mm. Through the amplitude-frequency curves of the three directions, it can be seen that there is a dangerous point of vibration before 50Hz, but the amplitude is relatively small, and it will not have an impact on the prototype; after 50Hz, the

amplitude of the curves gradually converges to zero. After 50Hz, the curve amplitude gradually tends to zero. Therefore, it can be assumed that there is no danger of resonance in the free mode.

Analyzing the harmonic response characteristics in the constrained mode, from the amplitude-frequency curves in three directions, it can be seen that at 11Hz and 12Hz, a larger amplitude will be generated in the x-direction and y-direction, respectively, and the amplitude of other frequency points is smaller, and the three curves are gradually converging to zero after 50Hz. Therefore, it is necessary to avoid the emergence of 11Hz and 12Hz excitation frequency by adjusting the rotational speed instruction, or reduce the residence time of the excitation frequency to avoid the danger caused by resonance.

## 5. Prototype System Integration and Control Scheme Optimization

The test system of the prototype is mainly composed of simulation verification module and physical flight verification system, the simulation verification module carries out attitude control simulation, and the physical flight test obtains flight data to provide guidance for control design. The simulation verification module consists of command module, controller, pneumatic module and six-degree-of-freedom model. The command module sends out commands, the PID controller processes and calculates the control commands, the pneumatic grinding block calculates the force and torque, and ultimately the six-degree-of-freedom model calculates the Eulerian angle of the prototype attitude information. The physical flight test system consists of ground station, remote control, ground equipment box and the prototype, the ground station monitors the state of the prototype, the remote control can send control commands to the prototype, the ground equipment box is equipped with a digital receiving and transmitting radios, to realize the ground station and the remote control and the flight control system on the prototype to transmit the information, the ground station to get the position and speed information processed by the gyroscope and speed sensor feedback after the controller. The ground station gets the position and speed information from the gyroscope and speed sensor after being processed by the controller.

The prototype itself consists of power system, control system and body structure, this section mainly completes the design of power system and control system of the prototype.

5.1. Power System Design

The power system should satisfy the relevant tests such as pull force and torque. The whole weight of the vertical take-off and landing UAV is 300 kg, and each main propeller power system needs to provide at least 150 kg of pulling force, and at the same time, it is required that the test aircraft hovering time is at least 7min, so it is necessary to select a reasonable propulsion system and function way. The key components of the power system include four parts: propeller, motor, electronic governor, and battery.

There are two kinds of propellers: variable pitch and fixed pitch. To analyze the dynamic model of the variable pitch propeller, the experimental conditions of the test site where this prototype is located have small wind speeds, which can be approximated that the propeller's operating state is in a static thrust state, based on the theory of leaf vein modeling of the variable pitch propeller. As Figure 16 shows the propeller at the radius of the corresponding leaf vein force state and velocity state. It indicates the pitch angle corresponding to the variable pitch propeller of this study, the angle of approach corresponding to the variable pitch propeller and the drag force and lift force on a single vane.
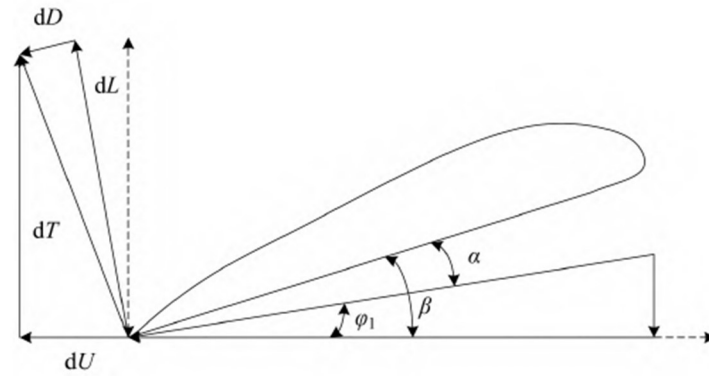
Figure 16. Forces and velocities exerted on propeller blade elements.

obtained from the basic foliation theory:

$$W_0 = \sqrt{v^2 + (rw)^2} \qquad (17)$$

Where: v is the incoming flow velocity; w is the pitch paddle rotational speed; W_0 is the combined velocity of the paddles by the airflow

$$dD = \frac{1}{2} C_D \rho W_0^2 c(r) dr \qquad (18)$$

$$dL = \frac{1}{2} C_L \rho W_0^2 c(r) dr \qquad (19)$$

Where: ρ is the air density; $C_L = C_{L\alpha}(\alpha - \alpha_0)$ is the lift coefficient; $C_D = C_{D0} + k C_{L\alpha}^2 (\alpha - \alpha_0)^2$ is the drag coefficient; α_0 is the zero lift head angle; $c(r)$ is the blade chord length at the paddle, which can usually be expressed as $c(r) = k_1 r$.

From the decomposition of the forces, the circular dF and dT tensile forces on the leaf vein are

$$dF = dL \sin \varphi_1 + dD \cos \varphi_1 \qquad (20)$$

$$dT = dL \cos \varphi_1 + dD \sin \varphi_1 \qquad (21)$$

Combining Equations. (19) to (21), the torque dM_p applied to the variable pitch at r can be obtained

$$dM_p = \frac{1}{2} \rho W_0^2 k_1 r^2 [C_L \sin \varphi_1 + C_D \cos \varphi_1] dr \quad (22)$$

For the torque M_p applied to the whole propeller is obtained by integrating Equation. (23):

$$M_p = N_b \cdot \int_0^R dM_p = N_b - \frac{1}{2} \rho k_1 \cdot$$
$$\{C_{L\alpha}(\alpha - \alpha_0) \sin \varphi_1 + [C_{D0} + k C_{L\alpha}^2 (\alpha - \alpha_0)^2] \cos \varphi_1\} \cdot \qquad (23)$$
$$\int_r^R [(rw)^2 + v^2] \times r^2 dr$$

Where: N_b is the number of paddle blades; r is the radius of the propeller disk;

For the torque T applied to the whole propeller, it is obtained by integrating Equation. (22):

$$T = N_b \cdot \int_0^R dT = N_b \cdot \frac{1}{2} \rho k_1 \cdot$$
$$\left\{ C_{L\alpha}(\alpha - \alpha_0)\cos\varphi_1 + [C_{D0} - kC_{L\alpha}^2(\alpha - \alpha_0)^2]\sin\varphi_1 \right\} \cdot \qquad (24)$$
$$\int_0^R [(rw)^2 + v^2] \cdot r \, dr$$

Assuming that the basic parameters of the propel k、k_1、$C_{L\alpha}$ and the external environmental parameters ρ are constants that do not vary with time, the accuracy of the model is verified by the ground test bed, and the incoming flow velocity $v = 0$, which is known for the current modeling is $\alpha_1 = 0, \beta = \alpha, \alpha_0 = 0$.

Equations. (24) and (25) can be deformed as:

$$M_p = \frac{1}{10}\rho N_b k_1 C_{D0} R^5 w^2 + \frac{1}{10}\rho N_b k_1 C_{L\alpha}^2 R^3 \beta^2 w^2 = q_1 w^2 + q_2 \beta^2 w^2 \qquad (25)$$

$$T = \frac{1}{10}\rho N_b k_1 C_{L\alpha} R^4 \beta w^2 = q_3 \beta w^2 \qquad (26)$$

The torque and thrust of the propeller can be obtained from the formula is only related to the pitch and rotational speed. According to this theoretical derivation of the formula combined with this selection of the propeller on the tension and torque plotted as shown in Figure 17, from Figure 17 it can be seen that the tension and torque is directly proportional to the square of the rotational speed, with the increase in rotational speed increases with the increase in the pitch angle increases with the increase in the pitch angle.
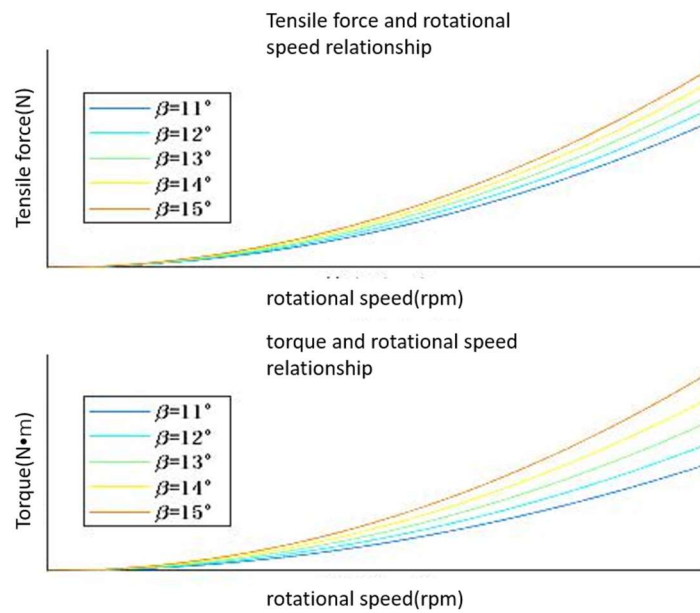
Figure 17. Effect of rotational speed and pitch angle on pulling torque.

So the variable pitch propeller can flexibly adjust the pulling force and torque, which can meet the more variable UAV load situation and complex environment. This design adopts a three-blade propeller with a diameter of 1.9m, which is a variable-pitch propeller, and the maximum pulling force that this propeller can provide meets the design index.

Brushless DC motor high efficiency, low loss, at the same time in the reliability, stability, adaptability, life of these aspects of the table are better than other motors, and the diameter of the propeller belongs to the large size propeller, so the selection of brushless motors is a large torque, low *KV* value of the motor, fixed selection of the EMRAX-268 motor, the motor external dimensions

268mm, the peak torque of 500 N The motor size is 268mm, and the peak torque is 500 N•m to meet the required torque parameters for this propeller selection.

The main function of the electronic speed controller is to convert the DC input into three-phase input of the motor, and at the same time to regulate the speed of the motor. According to the selected EMRAX-268 motor parameters, the maximum current of the motor is 320 A. Therefore, we choose the ESC DTI-HV500 with a maximum continuous current of 400 A. The ESC DTI-HV500 is the best choice for the propeller.

Battery selection should take into account factors such as lightweight, high efficiency and environmental protection, and the use of lithium batteries as the energy source of the UAV is a suitable choice. The battery is selected as Red Dot Battery 12S25C, with a standard voltage of 44.4V and a capacity of 12Ah.

5.2. Control System Design

Control system using DSP28377D control board, the control board contains a communication module, motor drive module, relay module, digital tube display module and signal processing module and other common modules, can realize the control system who design requirements. This design is only as a vertical takeoff and landing of an experiment, involving the main control and regulation part of the propeller speed control and regulation and current loop control and regulation, both of which use PID control methods. The control signal input form adopts two signal input forms, one is to use the ground station to input the speed command, with the receiver to receive the signal, to realize the motor speed control; the other is to use the remote control to input the speed signal, the same is the speed control command received by the receiver to realize the control of motor speed.
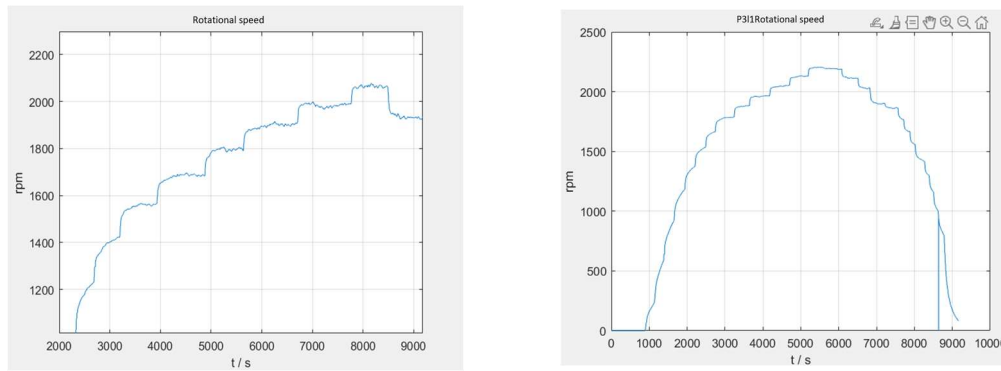
Firstly, the current loop parameters are controlled by PID control, and the parameters of the PID controller are optimized so that the current loop conforms to the current release situation to ensure that the system achieves the required stable power. The current loop control is controlled by PI control, firstly, the controller parameters are not modified first, the default parameters are simulated first, and then the controller parameters are optimized according to the effect of the experiment, and the simulated response curve of the system with different parameters is shown in Figure 18, which is optimized to the final controller parameters of proportionality coefficient of 3, and the integral link coefficient is 1.
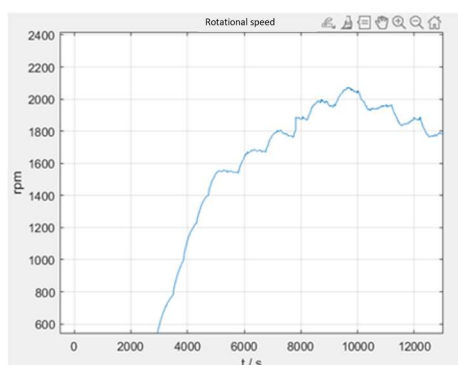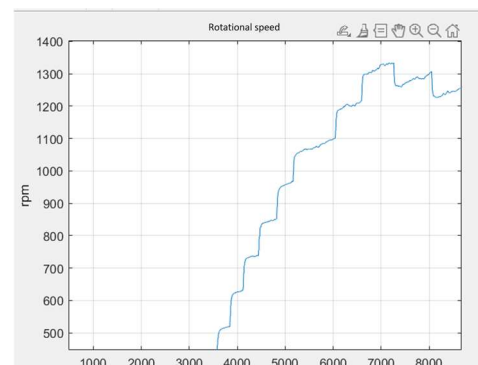
(a) P=0.4，I=0.6   (b) P=2，I=0.01

(c) P=3，I=0.5　　　　　　　　　　　　(d) P=3，I=0.01

Figure 18. Comparison of speed profiles with different controller parameters.

After adjusting the current loop parameters, the system can have a stable output power. Then optimize the design of the control parameters of the speed loop, establish the dynamics model of the electric propulsion system before designing the controller, and derive the transfer function of the electric propulsion system carrying the motor, which is directly connected to the propeller and has the same rotational speed. Combining the propeller dynamics model and the dynamics model of the motor, a nonlinear model of the electric propulsion dynamics is obtained, and the small influence of the brushless DC motor inductance on the control is neglected to obtain a simplified model of the electric propulsion of this design:

$$A_2 w + B_2 w + C_2 w^2 + D_2 w^2 \beta^2 = \sigma \qquad (27)$$

Where: the parameters to be recognized are respectively A_2, B_2, C_2, D_2.

Before the lithium battery is up to voltage, the battery voltage has a relatively small change in voltage throughout the operation of the electric propulsion system, so A_2, B_2, C_2, D_2 can be used as a constant to be recognized. The thrust and torque output equations of the variable pitch propeller are used as the power output of the system, and q_1、q_2、q_3 are the relevant parameters about the propeller blades, which can be obtained by experimental data identification. The nonlinear dynamics modeling equation set for the electrically driven variable pitch is:

$$\begin{cases} A_2 w + B_2 w + C_2 w^2 + D_2 w^2 \beta^2 = \sigma \\ M = q_1 w^2 + q_2 \beta^2 w^2 \\ T = q_3 \beta w^2 \end{cases} \qquad (28)$$

In the above modeling results, there are parameters to be identified, for this complex model structure, special points are selected to simplify it, when the pitch angle is zero, the rotational speed equation can be simplified to a section of inertial link with duty cycle as input and rotational speed as output, by means of time-domain identification, the electric propulsion system is inputted with the step signal, the output rotational speed of the system is collected, and the one-to-one corresponding data sets are imported into the Matlab system Recognition toolbox to obtain the system gain and time constant, it can be seen that the electric propulsion variable pitch system can be predicted to be a first-order inertial link after experimental identification, as shown in equation (30).

$$G = \frac{257.8}{0.311s + 1} \qquad (29)$$

After the transfer function of the electric propulsion system is determined, the speed loop is regulated based on the requirement of fast and stable speed control. This regulation adopts PID regulation, there are three regulation links: proportional, integral, differential. Set the initial controller
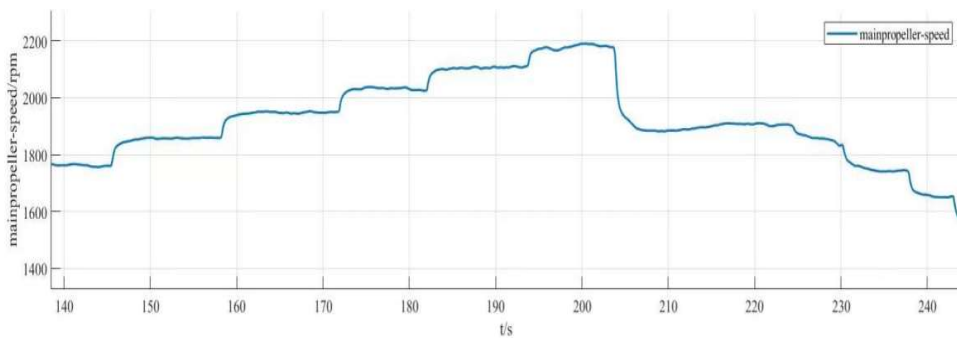
parameters for the proportional parameter 0.4 integral 0 differential 0.002 for a set of experiments, based on this simulation analysis to obtain the response data and further optimization of the parameters, to obtain several adjustments of the response curve in Figure 19.
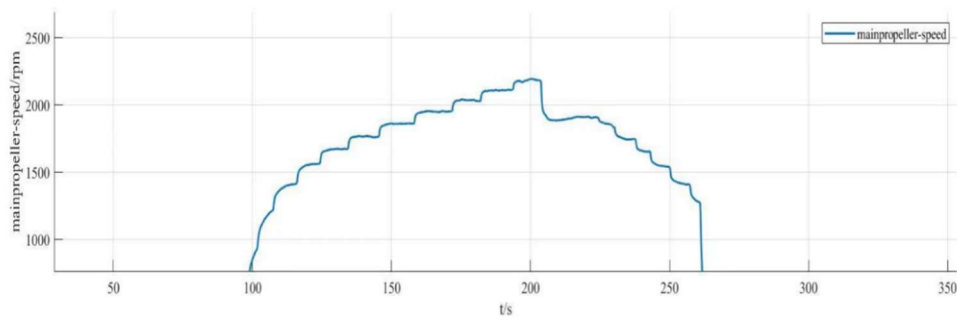

(a) P=0.4 i=0 d=0.002
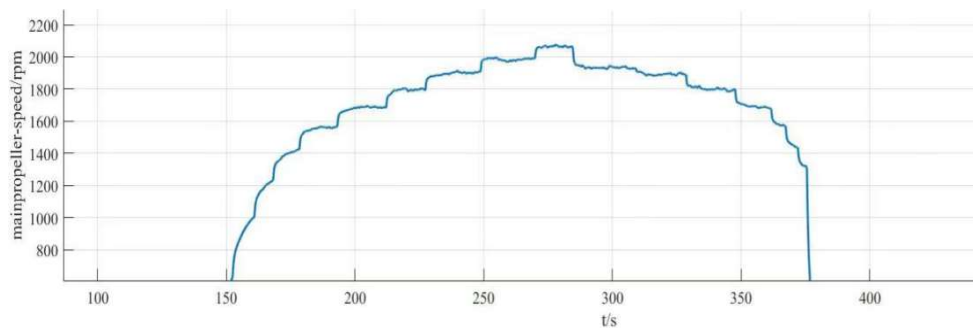
(b) P=0.8 i=0.02 d=0.002

(c) P=0.8 i=0.02 d=0.004

Figure 19. Velocity feedback curve of velocity loop with different controller parameters.

From the experimental response curve, it is concluded that: a in the response ability is good, but did not reach the target value, and the steady state error is large, when the command of 2100RPM is given, the response speed only reaches 2050RPM, which is not in line with the expectation; b in the response ability of the system to the improvement of the system, and at the same time, the steady state error decreases, but the fluctuation range of the speed curve is a little bit large; c in the response curve after amplification is still relatively stable, the fluctuation range is within 5RPM, and the steady state error is almost negligible, the speed ring regulation has met the experimental demand. In c, the response curve is still relatively stable after amplification, the fluctuation range is within 5RPM, the steady state error is almost negligible, and the speed ring adjustment has met the experimental demand.

Controller optimization is completed, test the actual control performance of the prototype. The ground station is designed using the QT platform, which is divided into the remote control end and the telemetry end. The remote control end inputs control commands to the UAV, mainly inputting the commanded RPM commands, and the telemetry end is used to receive the feedback data, which mainly includes the real-time values of the motor's RPM, voltage, current and temperature, etc. The remote control end is Futaba, which is used to control the UAV. The remote control is chosen to be Futaba T18SZ model, which has a frequency of 2.4GHz and up to 18 channels, together with a matching receiver. The results are shown in Figure 20, from the curve (a) and (b), it can be seen that the motor response performance meets the requirements when the speed command is issued through the ground station, the speed curve is tracked well, and the speed fluctuation range is within 5 rpm, which can realize the prototype speed stabilized at 1800 rpm and up to 2200 rpm. from Figure. (c) and (d), it can be seen that the propeller speed curve is in high agreement with the From Figure. (c) and Figure. (d), it can be seen that the propeller speed curve is highly consistent with the desired speed curve of the propeller, and the speed of the motor can be accurately controlled through the remote control instruction to realize the stable flight of the prototype.

(a)　　　　　　　　　　　　　　　　　　　　　　(b)

(c)　　　　　　　　　　　　　　　　　　　　　　(d)
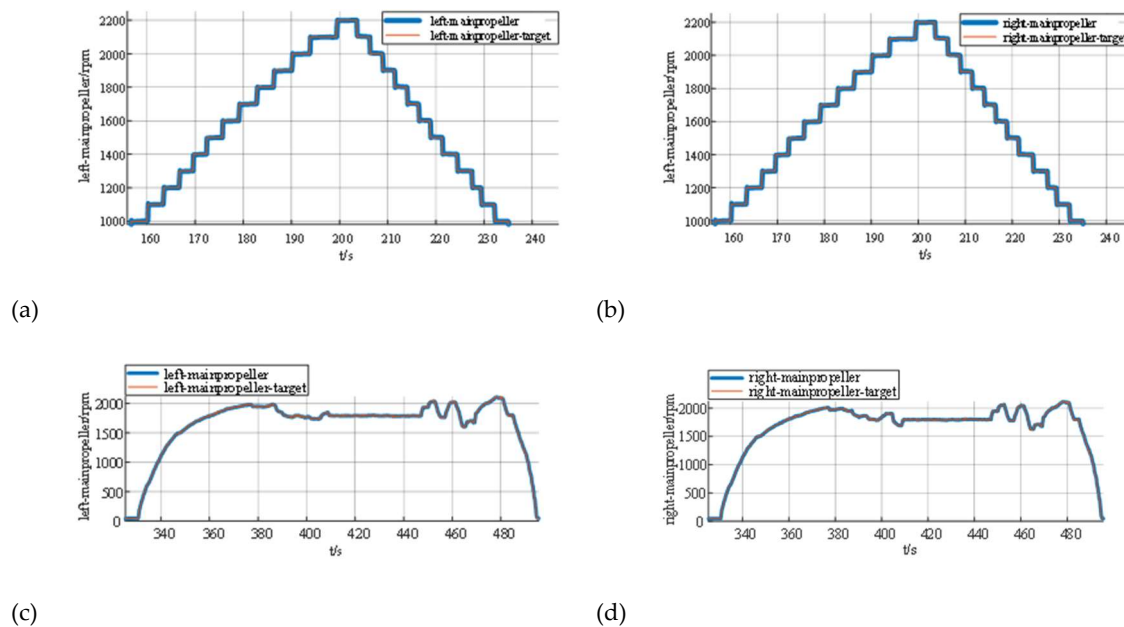
Figure 20. Dynamic response co-conditioning test results for real experiments.

After the experiment on the propeller speed tracking was completed, the attitude control of the test aircraft was carried out at low altitude by combining the serial PID control method, and after the completion of the experiment, the flight control data was downloaded, and the tracking curves shown in Figure 21, Figure 22 and Figure 23 were obtained, which showed the tracking curves of the test aircraft for the hovering experiment of tumbling, pitching and yawing.
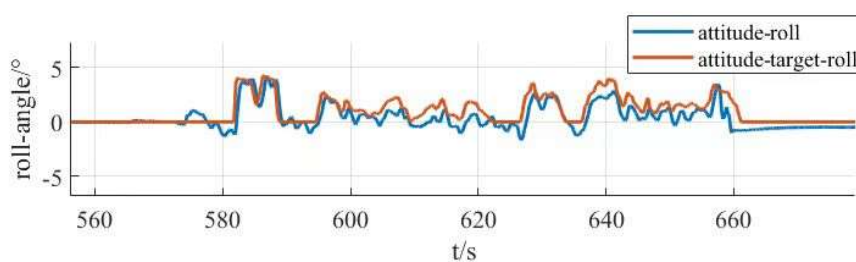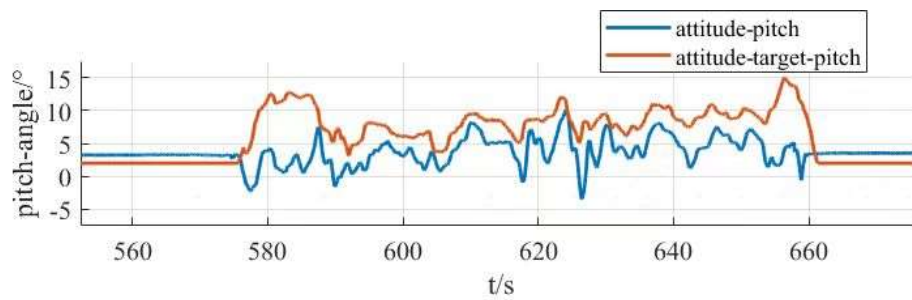

Figure 21. Roll Tracking Curve.
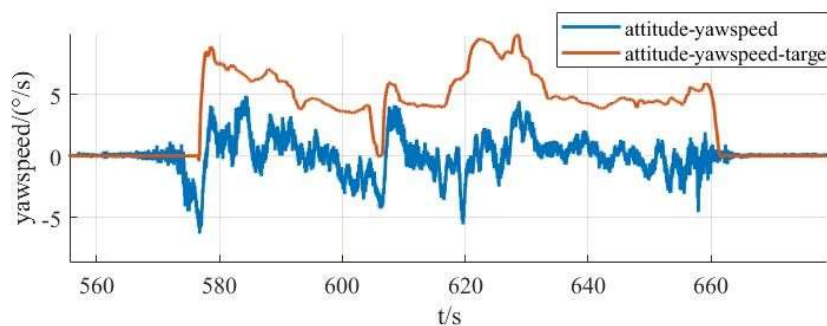
Figure 22. Pitch tracking curve.

Figure 23. Yaw tracking curve.

The tester roll control is good, the roll angle curve and the roll angle target curve trend is consistent, the maximum error is within 10%, within the acceptable range, the pitch angle and yaw angle curve and the target curve trend is consistent, the response speed is good, but there is a large error. Analyze the reason for the large error, the test aircraft has been in low altitude horizontal flight, the propeller and the ground will form a complex flow field, the formation of the ground effect, the test aircraft pitch is controlled by the rotational speed change of the tail rotor, the main rotor is subject to the ground effect is more pronounced, so the tail rotor to increase the lift is not enough to meet the requirements of the change in the pitch attitude; the test aircraft yaw is accomplished through the tail rotor's differential, the actual change in yaw curve value is much smaller than the target curve value. The yaw is accomplished by the differential movement of the tail rotor, and the actual change of yaw in the curve diagram is much smaller than the target curve value, which may be due to the fact that the rotational speed of the tail rotor is not enough to increase the lift, and on the other hand, the angle between the axis of the tail rotor and the z-axis of the fuselage coordinate system does not satisfy the requirements, and the y-axis direction of the y-axis direction of the y-axis direction of the y-axis is not enough.

In this section, the power system and control system of the prototype were designed. The propeller motor speed control, the flight attitude control of the prototype were carried out and the relevant control data were obtained through the ground station and the remote control, respectively, which provided the experimental data to guide the research of the tilt-rotor concept UAV.

6. Conclusions

Based on the reality that the research of tilt-rotor vertical take-off and landing UAV mostly stays in the theoretical research and verification, this paper designs a new tilt-rotor vertical take-off and landing UAV prototype and obtains the relevant design data of tilt-rotor vertical take-off and landing UAV through experiments, which provides a reliable data support and data reference for the future research of this type of UAV. This paper establishes a dynamic model of tilt-rotor vertical take-off and landing UAV according to the flight principle of quadrotor UAV, and completes the overall design of the prototype, material selection and dimension design according to the structural form

and design index of the UAV; analyzes the load and deformation response of the prototype according to the static analysis of finite element, and the maximum deformation of the prototype occurs at the edge of the wing beam and the main motor seat after the force is applied, with the maximum deformation value of 57.1mm, to achieve less than 3% of the design requirements, the maximum equivalent force of the prototype body structure is concentrated in the scaffolding fasteners, the maximum equivalent force value of 379.21MP, less than its minimum strength limit of 450 MPa, the maximum stress concentrated in the 6061 and 7075 aluminum alloy tubes 142.2 MPa, less than its minimum ultimate strength of 240 MPa and 455 MPa, this study The landing gear of the prototype is optimized by the unified objective method, and the beam length and angle of the landing gear after optimization are 579.15mm and 123.9°, respectively. Combining with the topology optimization module in the workbench, the motor seat and wing ribs are optimized by using the poi density method and the static structure module, and the maximum deformation of the motor seat after topology optimization and modification of the design is 0.08mm, and the maximum stress is 26.86 MPa, and the maximum deformation of the motor seat is 0.02mm, and the maximum deformation of the wing rib is 0.02 MPa. The maximum deformation of the wing ribs is 0.02mm, and the maximum stress is 12.94 MPa, which meets the requirements of the study; analyze the vibration response characteristics under the free mode and the vibration response characteristics under the constrained mode, and combined with the harmonic response analysis, it is concluded that the rotational speed command should avoid the occurrence of the excitation frequency of 11Hz and 12Hz, or reduce the excitation frequency to stay time to ensure the vibration safety performance of the prototype; according to the prototype flight According to the flight load of the test aircraft, the power system of the test aircraft is constructed and the control system is optimized. Through the actual flight test, the propeller speed tracking fluctuation of the test aircraft is within 5 rpm, and the error of the roll attitude of the test aircraft is within 10%. However, the test site of the experiments in this paper is limited, and for the sake of the experimental safety, the test aircraft only carries out the experiments in a low altitude, and the experimental results are affected by the ground effect, and the pitch attitude and yaw attitude control errors are larger, therefore, the future will be further developed. The experimental results are affected by the ground effect, and the pitch attitude and yaw attitude control errors are large, so the adaptive PID control will be further introduced in the future and higher altitude flight experiments will be carried out to eliminate the influence of the ground effect.

Institutional Review Board Statement: Not applicable.

Informed Consent Statement: Not applicable.

Data Availability Statement: Not applicable.

Conflicts of Interest: Not applicable.

References

1. Lu, K.; Liu, C.; Li, C.; Chen, R. Flight Dynamics Modeling and Dynamic Stability Analysis of TiltRotor Aircraft. International Journal of Aerospace Engineering. 2019,2019,15.

2. Kang, Y.; Park, B. J.; Cho, A.; Yoo, C. S.; Koo, S. O.; Tahk, M. J., Development of Flight Control System and Troubleshooting on Flight Test of a Tilt-Rotor Unmanned Aerial Vehicle. Int J Aeronaut Space 2016, 17, (1), 120-131.

3. Zhang, Q.; Zhang, J. J.; Wang, X. Y.; Xu, Y. F.; Yu, Z. L., Wind Field Disturbance Analysis and Flight Control System Design for a Novel Tilt-Rotor UAV. IEEE Access 2020, 8, 211401-211410.

4. Ducard, G. J. J.; Allenspach, M., Review of designs and flight control techniques of hybrid and convertible VTOL UAVs. Aerosp Sci Technol 2021, 118.

5. Su, J.; Su, C.; Xu, S.; Yang, X. A multi-body model of tilt-rotor aircraft based on Kane's method.International Journal of Aerospace Engineering. 2019,2019,2.

6. Kang, Y.S.; Park, B.; Cho, A.; Yoo, C.; Choi, S. Envelop expansion flight test of flight control systems for TR-60 tilt-rotor UAV. 2013 13th International Conference on Control, Automation and Systems (ICCAS 2013). 2013, 13, 1866-1871.

7. Barkai, S. M.; Rand, O.; Peyran, R. J.; Carlson, R. M. Modeling and analysis of tilt-rotor aeromechanical phenomena. Mathematical and Computer Modelling. 1998, 27(12), 17–43. doi:10.1016/s0895-7177(98)00071-5.

8. Papachristos, C.; Alexis, K.; Tzes, A. Design and experimental attitude control of an unmanned Tilt-Rotor aerial vehicle. 2011 15th International Conference on Advanced Robotics (ICAR).2011, 11, 465-471. doi:10.1109/icar.2011.6088631.

9. Chowdhury, A. B.; Kulhare, A.; Raina, G. Back-stepping control strategy for stabilization of a Tilt-rotor UAV. 2012 24th Chinese Control and Decision Conference (CCDC). 2012, 12, 3475-3480. doi:10.1109/ccdc.2012.6244555.

10. Cardoso, D. N.; Esteban, S.; Raffo, G., A new robust adaptive mixing control for trajectory tracking with improved forward flight of a tilt-rotor UAV. Isa T 2021, 110, 86-104.

11. Kumar, R.; R.Agarwal, S. Kumar M.; Modeling and Control of a Tethered Tilt-Rotor Quadcopter with Atmospheric Wind Model. IFAC PapersOnLine. 2021, 54-20, 463–468.

12. Al-Radaideh, A.; Sun, L. Self-localization of a tethered quadcopter using inertial sensors in a GPS-denied environment. 2017 International Conference on Unmanned Aircraft Systems (ICUAS).2017, 17, 271-277. doi:10.1109/icuas.2017.7991436.

13. Sato, M.; Muraoka, K., Flight Controller Design and Demonstration of Quad-Tilt-Wing Unmanned Aerial Vehicle. J Guid Control Dynam 2015, 38, (6), 1071-1082.

14. Panza, S.; Lovera, M.; Sato, M.; Muraoka, K., Structured μ-Synthesis of Robust Attitude Control Laws for Quad-Tilt-Wing Unmanned Aerial Vehicle. J Guid Control Dynam 2020, 43, (12), 2258-2274.

15. Yuksek, B.; Vuruskan, A.; Ozdemir, U.; Yukselen, M.A.; Inalhan, G. Transition flight modeling of a fixed-wing VTOLUAV. J. Intell. Robot. Syst. 2016, 84, 83–105.

16. Xie, M.; Xu, S.; Su, C.Y.; Feng, Z.Y.; Chen, Y.; Shi, Z.; Lian, J. An adaptive recursive sliding mode attitude control for tiltrotor UAV in flight mode transition based on super-twisting extended state observer. arXiv 2021, arXiv:2111.02046.

17. Liu, N. J.; Cai, Z. H.; Zhao, J.; Wang, Y. X., Predictor-based model reference adaptive roll and yaw control of a quad-tiltrotor UAV. Chinese J Aeronaut 2020, 33, (1), 282-295.

18. Papachristos, C.; Alexis, K.; Tzes, A., Dual-Authority Thrust-Vectoring of a Tri-TiltRotor employing Model Predictive Control. J Intell Robot Syst 2016, 81, (3-4), 471-504.

19. Irmawan, E.; Harjoko, A.; Dharmawan, A. Model, Control, and Realistic Visual 3D Simulation of VTOL Fixed-Wing Transition Flight Considering Ground Effect. Drones 2023, 7, 330. https://doi.org/ 10.3390/drones7050330.

20. Wei, Q. L.; Yang, Z. S.; Su, H. Z.; Wang, L. J., Online Adaptive Dynamic Programming for Optimal Self-Learning Control of VTOL Aircraft Systems With Disturbances. IEEE Trans. Autom. Sci. Eng 2024, 21, (1), 343-352.
21. El-Dalatony, A. M.; Attia, T.; Ragheb, H.; Sharaf, A. M., Cascaded PID Trajectory Tracking Control for Quadruped Robotic Leg. Int J Mech Eng Robot 2023, 12, (1), 40-47.